

# ACPV-Net: All-Class Polygonal Vectorization for Seamless Vector Map Generation from Aerial Imagery

WeiQin Jiao\* Hao Cheng George Vosselman Claudio Persello  
 Faculty of Geo-Information Science and Earth Observation (ITC)  
 University of Twente, The Netherlands  
 w.jiao@utwente.nl

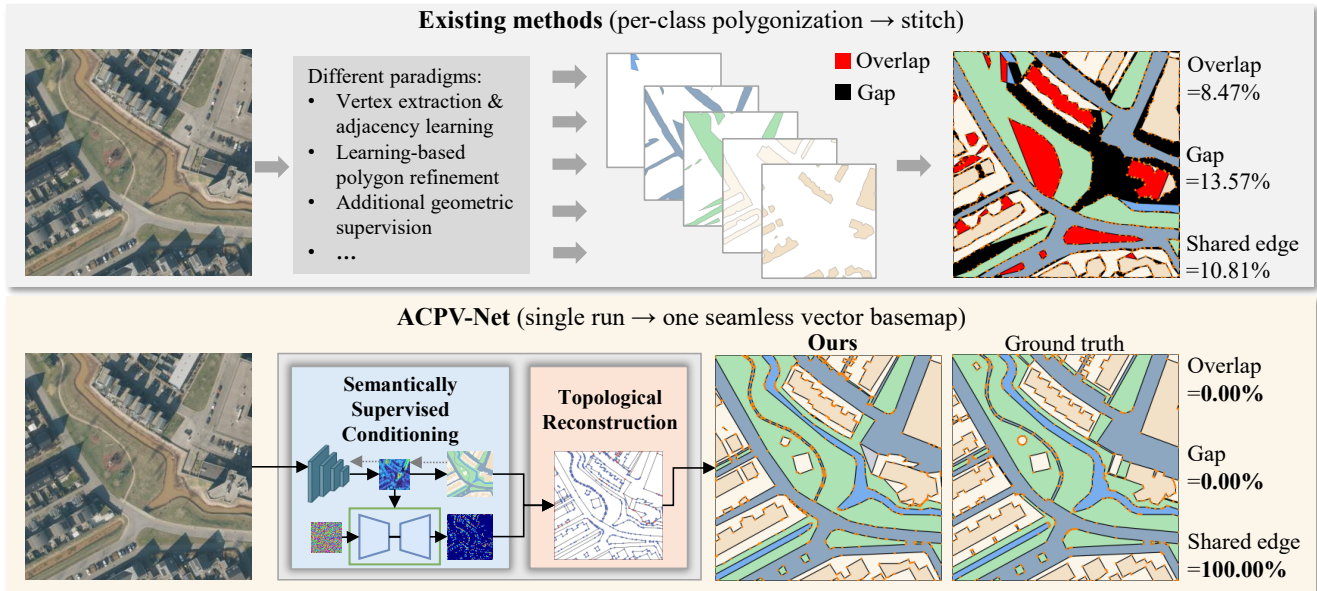


Figure 1. To generate an all-class vector basemap, existing single-class polygonization methods require per-class inference and stitching, resulting in gaps and overlaps across classes. ACPV-Net is the **first fully automatic framework** that produces a seamless basemap with **shared-edge consistency** and **avoids gaps and overlaps** in a single run.

## Abstract

We tackle the problem of generating a complete vector map representation from aerial imagery in a single run: producing polygons for all land-cover classes with shared boundaries and without gaps or overlaps. Existing polygonization methods are typically class-specific; extending them to multiple classes via per-class runs commonly leads to topological inconsistencies, such as duplicated edges, gaps, and overlaps. We formalize this new task as All-Class Polygonal Vectorization (ACPV) and release the first public benchmark, Deventer-512, with standardized metrics jointly evaluating semantic fidelity, geometric accuracy, vertex efficiency, per-class topological fidelity and global topological consistency. To realize ACPV, we propose ACPV-Net, a unified framework introducing a novel Semantically Supervised Conditioning (SSC) mechanism coupling semantic perception with geometric primitive generation, along with a topological reconstruction that enforces shared-edge consistency by design. While enforcing such strict topologi-

cal constraints, ACPV-Net surpasses all class-specific baselines in polygon quality across classes on Deventer-512. It also applies to single-class polygonal vectorization without any architectural modification, achieving the best-reported results on WHU-Building. Data, code, and models will be released at: <https://github.com/HeinzJiao/ACPV-Net>.

## 1. Introduction

A vector basemap, a.k.a. a topographic map, is a seamless, multi-class, vector representation of land cover, where each region is encoded as a polygon of a specific class, and adjacent polygons share precisely one common boundary without gaps or overlaps [6, 8, 12, 13, 18, 19, 27, 28]. Such basemaps form the foundation of national geospatial data infrastructures and are essential for cadastral management and land-use planning. Despite their importance, the production and maintenance of authoritative vector basemaps remain predominantly manual [7, 10, 11], leading to labor-

intensive, costly, and poorly reproducible workflows.

Learning-based polygonization methods [9, 15–17, 36, 38, 40, 42, 46] have advanced automated map vectorization but remain class-specific. They are typically run per class and then stitched to obtain a complete vector basemap. Such post-hoc stitching commonly breaks topology, leading to gaps, overlaps, and duplicated edges (Fig. 1), and thus falls short of the shared-edge and zero-gap requirements.

In this paper, we formalize this new task as *All-Class Polygonal Vectorization (ACPV)*: generating a single, globally consistent *planar partition* of the image domain into per-class polygons that satisfy strict topological constraints (formal definitions in Sec. 3). Compared with single-class polygon extraction, ACPV is substantially harder, as it requires unified reasoning over semantics and geometry under a globally consistent topological structure. Here, geometry refers to the geometric primitives that define polygonal structures, *e.g.*, edges, vertices, or equivalent structures, that encode region boundaries and support topological reconstruction. This challenge arises from five key factors: (i) **Semantic–geometric heterogeneity** (raster, categorical semantics vs. vector, continuous geometry) complicates joint optimization; (ii) **Strict alignment** is needed between semantic regions and geometric boundaries to preserve topological consistency; (iii) **Weak/ambiguous visual cues** in aerial imagery (shadows, occlusions, semantically ambiguous boundaries) demand reasoning beyond appearance; (iv) **Cartographic conventions** (heuristic rules on how densely to sample or simplify vertices along smooth boundaries) are difficult to encode explicitly in standard learning frameworks; and (v) **Global topological reconstruction** of a single planar partition with shared boundaries and no gaps/overlaps goes beyond per-class geometry.

To address these challenges, we introduce **ACPV-Net**, the first fully automatic framework that converts a single aerial image into a topologically consistent vector basemap, making a significant step toward fully automatic topographic mapping. We model geometry as discrete polygonal vertices, the atomic elements of polygonal structures, as Gaussian-mixture vertex heatmaps, allowing semantics and geometry to share the same raster domain. This distributional vertex representation enables the diffusion model to (1) learn cartographic sampling conventions that reflect human mapping heuristics, and (2) infer sparse, sharp vertex peaks under weak/ambiguous image cues such as shadows, occlusions, or semantically ambiguous boundaries. This generative, task-coupled geometry extraction stands in contrast to existing polygonal outline extraction methods [36, 38, 40, 46], which lack learned priors for cartographic conventions and degrade under weak image cues.

Our core mechanism, *Semantically Supervised Conditioning (SSC)*, directly supervises the diffusion conditioning stream with a semantic segmentation loss, enabling the

conditioning itself to learn task-coupled semantics. Unlike existing conditional diffusion pipelines [30, 39, 41, 43] that inject external conditions without explicit supervision, SSC turns the conditioning into an active guidance signal that enforces semantic–geometric alignment and focuses vertex generation within class-consistent regions. The coherent evidence (multi-class mask + vertex peaks) completes the ACPV formulation through a proposition-driven Planar Straight-Line Graph (PSLG) reconstruction, which provably ensures topological consistency by design rather than through heuristic post-processing (see Sec. 3, 4.2 for formal proof).

To evaluate this new task and framework, we establish **Deventer-512**, the first public benchmark for ACPV. Existing datasets either target single-class polygon extraction or provide multi-class raster masks without vector geometry, leaving no standard benchmark for ACPV. Deventer-512 fills this gap with high-resolution aerial imagery (0.3 m GSD) and fine-grained polygon annotations covering urban, suburban, and rural scenes under challenging conditions (shadows, occlusions, and semantically ambiguous boundaries). It is representative yet compact and computationally accessible ( $\sim 2k$  patches), comprising 1,716 training, 212 validation, and 220 testing patches, totaling 84,403 instances and 22,679 internal holes (the most complex polygon contains up to 708 vertices), covering five typical land-cover classes with diverse geometric complexity, suitable for assessing both semantic and geometric reasoning. A standardized evaluation protocol jointly measures semantic fidelity, geometric accuracy, vertex efficiency, per-class topological fidelity and global topological consistency. We also provide subsets for the above challenging conditions to enable robustness evaluation under weak/ambiguous evidence.

Our main contributions are summarized as follows:

- We address the vector basemap generation problem by formulating it as *All-Class Polygonal Vectorization (ACPV)*: generating a single, globally consistent *planar partition* of the image domain into per-class polygons that satisfy strict topological consistency.
- We introduce **ACPV-Net**, the first fully automatic framework that, in a single run, produces topologically consistent vector basemaps from aerial imagery.
- We release **Deventer-512**, the first public ACPV benchmark with high-resolution imagery, fine-grained polygons across five land-cover classes, a standardized evaluation protocol, and subsets for challenging conditions.
- ACPV-Net achieves gap-/overlap-free topology and significantly outperforms strong class-specific baselines across land-cover classes on Deventer-512. It also applies, without any architectural change, to single-class polygonal vectorization on the WHU-Building dataset while maintaining excellent performance.

## 2. Related work

**Single-class polygonal outline extraction.** Most learning-based methods [3, 9, 36, 38, 40, 46] address a single class, typically buildings, given their practical importance in mapping and the abundance of high-quality vector annotations. To construct a complete all-class map, their per-class results must be stitched post hoc, often introducing gaps, overlaps, or duplicated boundaries. Representative paradigms include learning-based polygon generation/refinement (*e.g.*, [29, 40]), vertex detection and adjacency learning (*e.g.*, [3, 38, 45, 46]), and additional geometric supervision such as attraction or frame fields (*e.g.*, [9, 36]). RoI-based variants [15, 17, 42] avoid heavy heads but still process cropped instances independently, hindering shared-edge reasoning and limiting scalability to area-covering or elongated classes. Recent works exploring class-agnostic or multi-class settings [25, 31, 38] remain primarily single-class in training or evaluation and combine per-class boundaries post hoc, without explicitly enforcing global topological consistency. In contrast, we pursue single-run, all-class polygonal vectorization that directly produces a topologically consistent planar partition of the image domain.

**Segmentation-to-vectorization cascades.** Multi-class land-cover mapping and semantic segmentation [20, 21, 23, 32–34, 44] output rasterized multi-class masks. Obtaining vectors often relies on geometry-driven, post-hoc simplifications such as Douglas–Peucker [5], applied per connected component of the mask. This often introduces duplicated or misaligned inter-class boundaries, gaps/overlaps, and redundant vertices, violating the formal constraints of a seamless vector basemap (specified in Sec. 3).

**Conditional diffusion for structured geometry.** Existing polygonization networks [3, 9, 36, 38, 40, 46] are predominantly *discriminative*, rely on discriminative visual cues to detect geometric structures such as vertices. Such formulations often struggle under weak/ambiguous cues (*e.g.*, shadows, occlusions, semantically ambiguous boundaries) and lack learned cartographic conventions. To overcome these limitations, diffusion-based generative models have shown potential to offer probabilistic reasoning that complements discriminative cues [16, 22]. However, existing conditional diffusion pipelines [30, 39, 41, 43] are primarily designed for generic visual synthesis, where external conditions (*e.g.*, images, texts, or sketches) are effective but lack explicit semantic supervision for structured geometry or semantic alignment. We fill this gap by introducing Semantically Supervised Conditioning (SSC), which directly supervises the conditioning branch with a semantic loss to guide vertex generation. This enables the model to learn cartographic conventions and maintain semantically aligned, sharp vertex peaks under weak image cues (see Sec. 6.3).

**Topology and planar graph reconstruction.** Topologi-

cal consistency is a fundamental requirement for seamless vector basemap generation, as formalized in cartographic and GIS standards that define planar partitions with shared boundaries and no gaps or overlaps [6, 13, 26, 27]. Although some polygonal outline extraction methods [3, 38, 46] incorporate graph-based designs to model vertex connectivity, and a few recent works (*e.g.* [4, 35]) introduce heuristic post-processing or topology-aware losses to alleviate local errors, they focus on local topological relationships rather than ACPV’s global topological consistency. To overcome this limitation, we introduce a proposition-driven planar straight-line graph (PSLG) reconstruction that ensures topological consistency, providing a globally consistent planar partition by construction (Sec. 4.2).

## 3. The ACPV task

We define ACPV (All-Class Polygonal Vectorization) as the task of producing a topology-consistent polygonal partition for all land-cover classes from an aerial image.

**Problem Definition** Let  $I : \Omega \rightarrow \mathbb{R}^k$  be an aerial image with  $k$  spectral channels ( $k = 3$  for RGB) and  $\mathcal{C}$  be a finite land-cover class set with  $|\mathcal{C}| = C$ , ACPV seeks a labeled polygonal partition  $\{\mathcal{P}_c\}_{c \in \mathcal{C}}$  of the spatial domain  $\Omega$  that satisfies the following constraints:

**(a) Planar partition.** Polygon interiors are disjoint, and the union of all polygons fills the whole domain  $\Omega$ :

$$\begin{aligned} \text{int}(p_i) \cap \text{int}(p_j) &= \emptyset \quad \forall i \neq j, \\ \bigcup_c \bigcup_{p \in \mathcal{P}_c} \text{int}(p) &= \Omega. \end{aligned} \quad (1)$$

where  $\mathcal{P}_c$  denotes the set of polygons labeled by class  $c$  and  $\text{int}(p)$  is the interior of polygon  $p$ .

**(b) Shared boundaries.** Any two adjacent polygons share one identical boundary segment, and no duplicate or parallel copies of the same boundary exist.

**(c) Zero gap/overlap.** Each point in  $\Omega$  belongs to exactly one polygon, except along shared boundaries.

**(d) Linear geometry.** Each polygon boundary is a finite union of simple piecewise-linear chains (outer ring plus optional holes), without self-intersections.

**(e) Semantic consistency.** Each polygon carries exactly one label  $c \in \mathcal{C}$ , and label transitions occur only across shared boundaries.

**(f) Minimal vertex redundancy.** Each polygon boundary is represented in a canonical, vertex-minimal form: no duplicate consecutive vertices or geometrically redundant points are allowed along any linear segment; vertex reduction must preserve the polygon’s geometry and topology.

## 4. Method

We aim to generate a seamless, topology-consistent vector basemap from a single aerial image  $I$  – a single planar parti-

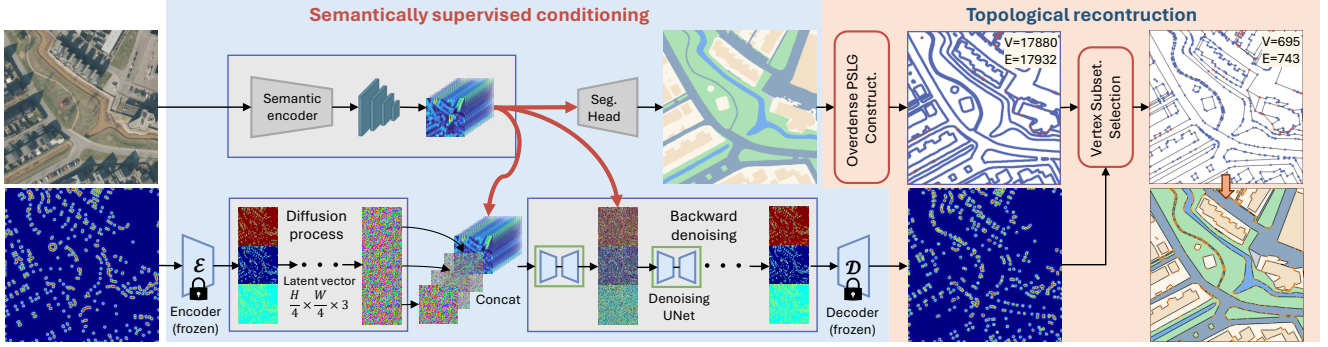


Figure 2. Overview of ACPV-Net. It unifies semantically supervised conditioning and proposition-driven topological reconstruction: the former produces coherent semantic–geometric evidence through diffusion-based vertex generation under semantic supervision, the latter deterministically reconstructs a topology-consistent vector basemap via overdense PSLG construction and vertex-guided subset selection.

tion of the image domain into per-class polygons satisfying the ACPV constraints (Sec. 3). We propose **ACPV-Net**, as shown in Fig. 2, a *unified* framework with two tightly coupled components:

- **Semantically supervised conditioning (SSC).** We choose vertices as the geometric primitives for constructing the vector basemap. Vertices of an aerial image are encoded as a *Gaussian-mixture heatmap* and reconstructed in latent space with a diffusion model. The conditioning stream is *explicitly* supervised by a semantic segmentation loss, so that semantics guide vertex generation and enforce semantic–geometric alignment.
- **Proposition-driven topological reconstruction.** From the coherent evidence  $(\hat{M}, \hat{Y})$  with semantic masks  $\hat{M}$  and vertex heatmap  $\hat{Y}$ , we reconstruct polygons through a *planar straight-line graph (PSLG)*–based algorithm derived from a sufficient condition that *ensures* global topological consistency by design.

#### 4.1. Semantically supervised conditioning

**Distributional vertex modeling.** Let  $y \in [0, 1]^{H \times W}$  be a Gaussian-mixture vertex heatmap (peaks centered at annotated corners). We encode  $y$  into a latent  $z_0 = \mathcal{E}(y) \in \mathbb{R}^{C_s \times H' \times W'}$  ( $H' = H/4$ ,  $W' = W/4$ ) using a pretrained variational autoencoder (VAE) from [30]. As verified in the supplementary, the pretrained VAE preserves vertex-peak information with negligible degradation, making fine-tuning unnecessary; thus, it is kept frozen during training.

**Task-coupled conditioning.** A semantic encoder  $S_\psi(I) \in \mathbb{R}^{C_s \times H' \times W'}$  provides conditioning features at the same spatial scale as  $z_0$ . Unlike generic conditional pipelines [30, 39, 41, 43], we *explicitly* supervise  $S_\psi$  with a segmentation loss via a lightweight segmentation head, so that the conditioning carries discriminative semantics aligned with the downstream vertex generation.

**Denosing objective.** With forward noising  $q(z_t | z_{t-1})$  and schedule  $\{\beta_t\}_{t=1}^T$ , the latent diffusion model predicts the

clean latent  $\hat{z}_0$  from the noisy input  $z_t$  conditioned on semantic features  $S_\psi(I)$ :

$$\hat{z}_0 = \phi_\theta(z_t, t, \text{Cond}(S_\psi(I), z_t)). \quad (2)$$

where  $S_\psi$  is trained *jointly* with the denoiser under the unified loss:

$$\mathcal{L}_{\text{SSC}} = \lambda_\epsilon \mathbb{E} \|\epsilon - \epsilon_\theta(\cdot)\|_1 + \lambda_0 \mathbb{E} \|z_0 - \hat{z}_0\|_1 + \lambda_{\text{seg}} \mathcal{L}_{\text{seg}}(\hat{M}, M), \quad (3)$$

where  $\mathcal{L}_{\text{seg}}$  is applied to the semantic prediction  $\hat{M}$ . At inference, iterative denoising yields  $\hat{z}_0$ , which is decoded to a vertex heatmap  $\hat{Y} = \mathcal{D}(\hat{z}_0)$ . The pair  $(\hat{M}, \hat{Y})$  constitutes coherent semantic–geometric evidence, with vertices spatially aligned with class boundaries in the semantic mask and covering key geometric corners. This coherent evidence serves as the input for the proposition-driven topological reconstruction detailed in Sec. 4.2.

#### 4.2. Proposition-driven topological reconstruction

We reconstruct a single planar partition from  $(\hat{M}, \hat{Y})$ . We first formalize a *sufficient condition* under which the reconstructed planar partition satisfies all ACPV constraints (a)–(f) (see Sec. 3); we then derive a *deterministic* algorithm that satisfies this condition by construction. An overview of the process is shown in Fig. 2.

**Proposition 1** (Sufficient condition for ACPV compliance). Let  $G = (V, E)$  be a *planar straight-line graph* embedded in  $\mathbb{R}^2$ . Suppose that:

- Each edge  $e \in E$  lies along a label-transition boundary in the multi-class mask  $\hat{M}$ , and the two faces adjacent to  $e$  have distinct semantic labels; and
- The vertex set  $V$  consists exclusively of *geometric key-points*, that is, vertices whose removal would alter the polygon’s topology or geometric structure.

Then the polygonal partition obtained by tracing all face boundaries on  $G$  and assigning face labels according to  $\hat{M}$  satisfies all ACPV constraints (a)–(f). A complete proof is provided in the supplementary.

**Deterministic algorithm.** We enforce the two premises in Proposition 1 by construction:

(1) **Overdense PSLG construction.** From the predicted multi-class mask  $\hat{M}$ , we extract all label-transition loci on the pixel-center lattice (including image borders) and connect adjacent transition pixels into one-pixel-wide boundary chains. Each transition pixel is treated as a vertex, and adjacent pairs form edges, resulting in a lattice-aligned planar straight-line graph  $G = (V, E)$ . We deliberately keep all transition locations without any thinning or pruning, making  $G$  *globally overdense*, a superset covering all admissible boundary positions required by Proposition 1 Condition (i). This step establishes the planar scaffold on which the subsequent vertex-guided selection operates to satisfy Proposition 1 Condition (ii).

(2) **Vertex-guided subset selection.** We decompose the overdense PSLG  $G = (V, E)$  at anchor vertices ( $\deg(v) \neq 2$ ) into anchor-bounded polylines. Discrete vertex peaks  $\hat{V}_p$  extracted from  $\hat{Y}$  are projected onto their nearest PSLG loci within a fixed radius  $\tau$  and ordered by arc length. The anchors and the projected keypoints are preserved to form simplified polylines that retain boundary geometry while removing redundant vertices. This step is designed to realize Proposition 1 Condition (ii). Together with Step (1), which satisfies Condition (i), it yields a simplified PSLG. Tracing the faces of this PSLG and assigning labels from  $\hat{M}$  produces the final vectorized map.

All operations are deterministic and use only protocol-level constants (e.g.  $\tau$ ), without dataset-specific tuning.

## 5. The ACPV Benchmark

Automated polygonal outline extraction has long relied on single-class datasets (e.g., Inria [24], WHU-Building [14]), where only one class is vectorized and topology across land-cover classes is ignored. Conversely, existing multi-class land-cover benchmarks (e.g., LoveDA [33], ISPRS Vaihingen/Potsdam [1, 2]) provide only raster masks, lacking vector geometry. No public dataset currently supports evaluating ACPV, defined in Sec. 3, as an all-class polygonal vectorization task with strict topological constraints, nor provides standardized *global topology-consistency metrics* for such evaluation. As shown in Table 1, the proposed **Deventer-512** fills this gap by providing high-resolution aerial imagery with topologically valid, multi-class vector annotations forming a single planar partition per patch, and a standardized evaluation protocol that measures both per-class polygonal quality and global topological consistency.

**Deventer-512** is built from ortho-rectified aerial RGB imagery over the Deventer region in the eastern Netherlands, acquired from the national cadastral mapping service (*Kadaster*) at a ground sampling distance of 0.3 m. All annotated polygons within each  $512 \times 512$  patch are organized to form a topology-consistent planar partition with shared

Table 1. Comparison of representative datasets for **polygonal outline extraction** (top) and **land-cover mapping** (bottom). “V” indicates vector annotations; “S” shared-edge consistency; “T” global topology-consistency metrics; and “C” cadastral-aligned boundaries (as opposed to purely visual contours).

Dataset	Multi-class	V	S	T	C
Inria [24]	✗	✗	✗	✗	✓
WHU-Building [14]	✗	✓	✗	✗	✓
ISPRS Vaihingen [2]	✓	✗	✗	✗	✗
ISPRS Potsdam [1]	✓	✗	✗	✗	✗
LoveDA [33]	✓	✗	✗	✗	✗
<b>Deventer-512 (Ours)</b>	✓	✓	✓	✓	✓

boundaries (Sec. 3). Polygon annotations originate from official cadastral data and are refined through a topology-validation pipeline to ensure *global topological consistency* (details in the supplementary material).

The dataset contains five land-cover classes, *i.e.* *buildings*, *roads*, *vegetation*, *water*, and *unvegetated area*, each represented as a topologically valid polygon set. It comprises 1,716 training, 212 validation, and 220 testing patches, totaling 84,403 instances and 22,679 internal holes, with the most complex polygon containing up to 708 vertices. The polygons exhibit higher geometric complexity and vertex density than single-class building datasets, where object geometry is relatively simple. They are delineated following cadastral or administrative boundaries rather than purely visual ones, which introduces semantic–visual discrepancies, leading to semantically ambiguous boundaries that make the dataset particularly challenging. A more detailed description of the dataset is provided in the supplementary.

### 5.1. Evaluation protocol and baselines

**Evaluation Metrics.** We evaluate polygonal quality under a unified metric suite spanning: *semantic fidelity*, *geometric accuracy*, *vertex efficiency*, and *topological consistency*. Details are provided in the supplementary material.

**Baselines.** We evaluate five representative state-of-the-art polygonization methods over the three major paradigms discussed in Sec. 2: *DeepSnake* [29] (a learned polygonization module based on active contour evolution), *FFL* [9] (frame-field-guided polygonization), *TopDiG* [38] (transformer-based vertex detection and adjacency learning), *HiSup* [36] (hierarchical attraction-field supervision), and *GCP* [40] (a global contour proposal network with transformer-based polygon refinement). They span learned polygon refinement, vertex extraction and adjacency learning, and geometric-field modeling, ensuring comprehensive coverage of existing polygonization paradigms. They are trained and evaluated on Deventer-512 using identical patch-based settings and evaluation metrics.

Table 2. **Global topological consistency on Deventer-512.** Metrics include gap rate (Gap), inter-class overlap rate (Inter), intra-class overlap rate (Intra) and shared-edge consistency rate (Shared). Best and second-best values are highlighted in **bold** and underlined, respectively. All percentage values are reported to two decimal places.

Method	Gap ↓	Inter ↓	Intra ↓	Shared ↑
DeepSnake [29](CVPR '20)	12.41	68.86	51.16	<u>38.73</u>
FFL [9](CVPR '21)	5.48	29.17	<u>0.08</u>	9.20
TopDiG [38](CVPR '23)	8.47	13.57	<b>0.00</b>	10.81
HiSup [36](ISPRS '23)	<u>5.43</u>	<u>4.50</u>	<b>0.00</b>	25.73
GCP [40](TGRS '25)	8.75	10.39	41.91	20.25
ACPV-Net (Ours)	<b>0.00</b>	<b>0.00</b>	<b>0.00</b>	<b>100.00</b>

## 6. Experiments

### 6.1. ACPV on Deventer-512

We first evaluate the output vector basemap as a whole to verify compliance with the ACPV constraints in realizing seamless all-class vector map generation from aerial imagery. As shown in Table 2, when the single-class outputs of baselines are stitched together, they consistently exhibit non-zero inter- and intra-overlap rates, whereas ACPV-Net achieves zero measured gap and overlap rates and 100% shared-edge consistency, confirming the seamless nature of the generated vector basemap. Detailed per-class overlap statistics are reported in the supplementary material.

We further analyze per-class performance by extracting polygons of each land-cover class from this basemap and compare them with state-of-the-art single-class polygonization methods, each applied separately to individual land-cover classes. As shown in Table 3, ACPV-Net produces all classes in one pass and achieves consistent improvement across all five classes in semantic fidelity, geometric accuracy, topological fidelity, and vertex efficiency, without any class-specific tuning, except for a slightly higher MTA on water (42.63 ours vs. 42.22 HiSup). This difference is likely due to our more compact vertex representation measured in N-ratio (0.92 ours vs. 3.26 HiSup) for representing irregular curved water body boundaries.

Figure 3 presents three representative scenes from the Deventer-512 test set: *urban*, *suburban*, and *rural areas*. These examples also cover challenging visual conditions such as shadow, partial occlusion, and semantically ambiguous boundaries. ACPV-Net predicts more accurate vector maps than the other models, illustrating the robustness of ACPV-Net under weak visual cues. Additional qualitative comparisons under more visual conditions and baselines are provided in the supplementary material.

### 6.2. Single-class Polygonal Vectorization

To further validate the applicability of ACPV-Net beyond multi-class mapping, we directly apply the same archi-

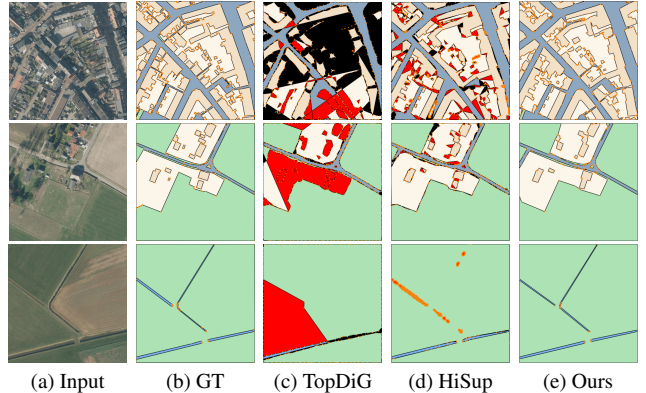


Figure 3. Qualitative comparison on Deventer-512. The three rows show representative urban, suburban, and rural scenes, respectively. From left to right: aerial imagery, ground truth, TopDiG [38], HiSup [36], and Ours. Land-cover classes are color-coded; polygon outlines are drawn in black, vertices are highlighted with orange dots, and inter-class overlaps and gaps are marked in red and black, respectively.

ecture to single-class polygonal vectorization without any structural modification. We select the WHU-Building dataset [14] for this experiment because *building* is the most common and structurally representative category in aerial imagery, and the dataset provides large-scale, high-resolution images with reliable annotations. As summarized in Table 4, ACPV-Net achieves the best-reported results on WHU-Building against building-specific single-class polygonization baselines, demonstrating that ACPV-Net is not limited to seamless multi-class vector map generation. It also serves as a unified and flexible framework for single-class polygonal outline extraction. Representative visual results are provided in the supplementary material.

It is worth mentioning that, to examine cross-region robustness, we apply the same model trained on Deventer-512 to high-resolution aerial imagery from cities in other countries and sensors without fine-tuning. The results (see supplementary) show consistent topological validity and reasonable polygon regularity in visually similar regions.

### 6.3. Ablation Studies

We conduct comprehensive ablations to verify the effectiveness of each key design component in ACPV-Net. Specifically, we analyze (i) how semantically supervised conditioning (SSC) suppresses artifacts and enhances semantic-geometric alignment, (ii) how distributional vertex modeling via latent reconstruction improves robustness and vertex precision under weak/ambiguous visual cues, and (iii) how the deterministic reconstruction ensures topological consistency by design. All experiments are performed on Deventer-512 under identical settings (see implementation details in the supplementary).

Table 3. **Quantitative comparison on Deventer-512**. Best and second-best values are highlighted in **bold** and underlined, respectively. APLS is evaluated only on elongated classes (roads and water bodies).

Class	Method	Semantic fidelity		Vertex efficiency		Geometric accuracy		Topological fidelity		
		IoU $\uparrow$	B-IoU $\uparrow$	N-ratio $\rightarrow$ 1	C-IoU $\uparrow$	PoLiS $\downarrow$	MTA $\downarrow$	APLS $\uparrow$	$\chi$ -Err $\downarrow$	$\beta$ -Err $\downarrow$
Road	DeepSnake [29] (CVPR '20)	10.35	7.90	74.91	4.58	33.18	53.38	64.85	7.82	10.11
	FFL [9] (CVPR '21)	62.00	58.08	3.74	42.28	11.48	44.05	78.53	15.31	15.40
	TopDiG [38] (CVPR '23)	58.75	55.95	1.80	44.06	10.28	44.27	70.65	5.90	6.54
	HiSup [36] (ISPRS '23)	73.92	69.29	2.00	57.36	4.97	44.84	81.06	5.16	5.45
	GCP [40] (TGRS '25)	59.93	56.58	0.86	44.96	9.18	49.19	73.00	4.38	5.18
	<b>Ours</b>	<b>76.01</b>	<b>73.32</b>	<b>1.07</b>	<b>68.22</b>	<b>4.44</b>	<b>43.85</b>	<b>83.52</b>	<b>3.68</b>	<b>4.04</b>
Building	DeepSnake [29] (CVPR '20)	34.24	29.96	30.00	9.64	4.41	50.38	—	7.39	8.45
	FFL [9] (CVPR '21)	63.69	60.91	8.69	40.56	3.21	48.12	—	39.71	42.60
	TopDiG [38] (CVPR '23)	72.56	69.03	1.07	63.12	3.37	45.97	—	7.21	8.37
	HiSup [36] (ISPRS '23)	81.22	78.06	1.55	70.60	2.23	42.59	—	6.82	7.70
	GCP [40] (TGRS '25)	73.97	70.41	1.79	58.59	2.91	47.37	—	6.84	7.45
	<b>Ours</b>	<b>82.08</b>	<b>79.50</b>	<b>1.00</b>	<b>77.24</b>	<b>1.76</b>	<b>39.39</b>	—	<b>2.32</b>	<b>2.72</b>
Unvegetated	DeepSnake [29] (CVPR '20)	21.06	10.84	68.93	3.31	17.32	53.90	—	8.25	11.85
	FFL [9] (CVPR '21)	43.91	35.56	30.62	24.99	19.27	47.40	—	84.35	91.59
	TopDiG [38] (CVPR '23)	49.26	39.92	0.77	40.61	12.73	48.44	—	6.30	10.28
	HiSup [36] (ISPRS '23)	61.46	55.37	1.93	51.79	8.66	47.17	—	4.22	5.34
	GCP [40] (TGRS '25)	47.85	38.39	1.23	41.09	10.71	53.67	—	6.10	8.09
	<b>Ours</b>	<b>66.89</b>	<b>61.51</b>	<b>1.09</b>	<b>61.79</b>	<b>6.41</b>	<b>46.79</b>	—	<b>2.80</b>	<b>3.62</b>
Vegetation	DeepSnake [29] (CVPR '20)	51.18	25.88	58.81	3.70	16.63	51.89	—	16.89	17.96
	FFL [9] (CVPR '21)	61.19	39.18	4.12	29.23	15.46	46.35	—	33.65	33.95
	TopDiG [38] (CVPR '23)	70.02	49.64	2.67	44.09	11.35	45.79	—	9.31	11.43
	HiSup [36] (ISPRS '23)	75.70	57.85	3.54	46.07	7.51	41.86	—	8.53	9.70
	GCP [40] (TGRS '25)	70.37	49.65	2.57	45.24	9.00	49.29	—	12.97	14.05
	<b>Ours</b>	<b>80.05</b>	<b>64.50</b>	<b>0.98</b>	<b>67.55</b>	<b>6.22</b>	<b>41.43</b>	—	<b>6.62</b>	<b>7.53</b>
Water	DeepSnake [29] (CVPR '20)	27.27	20.93	116.05	14.87	14.62	53.55	56.05	5.57	6.83
	FFL [9] (CVPR '21)	54.73	47.02	5.53	41.72	7.92	44.91	61.22	11.24	11.29
	TopDiG [38] (CVPR '23)	43.23	39.65	0.36	33.61	9.14	43.58	30.75	1.93	2.05
	HiSup [36] (ISPRS '23)	64.84	58.23	3.26	51.79	4.29	42.22	58.40	1.77	1.86
	GCP [40] (TGRS '25)	52.74	45.87	1.08	44.52	5.00	46.24	60.85	1.55	1.64
	<b>Ours</b>	<b>67.96</b>	<b>62.05</b>	<b>0.92</b>	<b>59.53</b>	<b>3.83</b>	<b>42.63</b>	<b>68.81</b>	<b>1.28</b>	<b>1.34</b>

Table 4. Quantitative comparison on WHU-Building. Best values are in **bold** and second-best values are underlined.

Method	Sem. fidelity		Vertex efficiency		Geo. accuracy		Topo. fidelity	
	IoU $\uparrow$	B-IoU $\uparrow$	N-ratio $\rightarrow$ 1	C-IoU $\uparrow$	PoLiS $\downarrow$	MTA $\downarrow$	$\chi$ -Err $\downarrow$	$\beta$ -Err $\downarrow$
DeepSnake [29]	71.39	64.10	2.05	54.21	2.17	46.85	4.43	6.29
FFL [9]	80.86	74.63	3.68	46.09	2.13	38.86	12.33	14.88
TopDiG [38]	83.79	77.73	1.95	62.25	1.99	38.82	2.13	2.56
HiSup [36]	<u>87.63</u>	<u>82.82</u>	<u>1.93</u>	<u>67.15</u>	<u>1.40</u>	<u>35.27</u>	<u>1.95</u>	<u>2.28</u>
GCP [40]	83.28	77.58	2.11	60.51	1.66	34.96	3.20	4.39
<b>Ours</b>	<b>88.50</b>	<b>83.39</b>	<b>1.07</b>	<b>81.45</b>	<b>1.38</b>	<b>34.85</b>	<b>1.60</b>	<b>1.81</b>

**SSC and Distributional Vertex Modeling.** We conduct two controlled experiments to isolate the effects of (i) explicit semantic supervision (SSC) and (ii) distributional vertex modeling through latent reconstruction.

(i) **No explicit semantic supervision (No-SSC).** We disable the gradient flow of the segmentation loss  $\mathcal{L}_{\text{seg}}$  to the conditioning encoder  $S_{\psi}$ , so that its features are optimized only through the diffusion objective. This setting reduces the model to a typical conditional diffusion setup (e.g. [30, 39, 41, 43]) without explicit task-specific supervision. The segmentation head remains active, producing  $\hat{M}$  for fair comparison. Without explicit semantic guidance, the model produces numerous false-positive vertex activations, many of which appear inside homogeneous regions rather than along class-consistent boundaries (see Fig. 4). We quantify this misalignment using the *Vertex–Boundary*

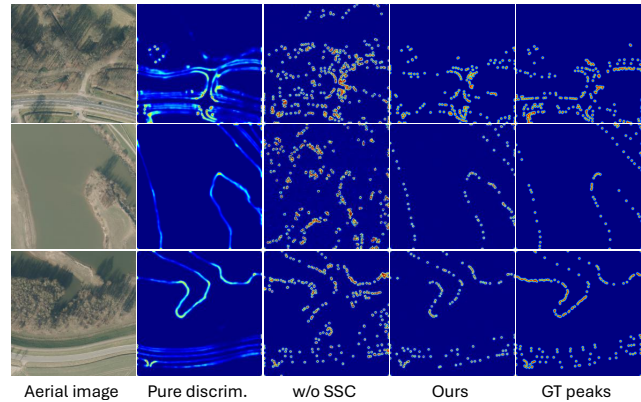


Figure 4. Vertex activations under weak/ambiguous visual cues and along smooth boundaries (cartographic convention cases). From left to right: aerial image, pure discriminative decoding, without semantic supervision (No-SSC), ours, and ground truth.

*Alignment* ( $V2B\delta$ ) metric, the fraction of predicted vertices that fall within  $\tau$  pixels of their class-consistent boundaries. As shown in Table 5, removing  $\mathcal{L}_{\text{seg}}$  leads to a clear drop in alignment, confirming that explicit semantic supervision enhances semantic–geometric consistency.

(ii) **Pure discriminative decoding.** To assess the impact of distributional vertex modeling, we replace the latent reconstruction with a direct pixel-space decoder (*pure dis-*

Table 5. Vertex–Boundary Alignment (V2B@ $\delta$ ) comparison between *No-SSC* and *Full SSC*. Global boundaries are computed as multi-class label transitions from the raster mask. **Avg(2,4,6)** denotes the mean of V2B@2, @4, and @6.

Variant	V2B@2 $\uparrow$	V2B@4 $\uparrow$	V2B@6 $\uparrow$	Avg@2,4,6 $\uparrow$
No-SSC	0.38	0.48	0.53	0.46
<b>Full SSC (ours)</b>	<b>0.78</b>	<b>0.87</b>	<b>0.90</b>	<b>0.85</b>

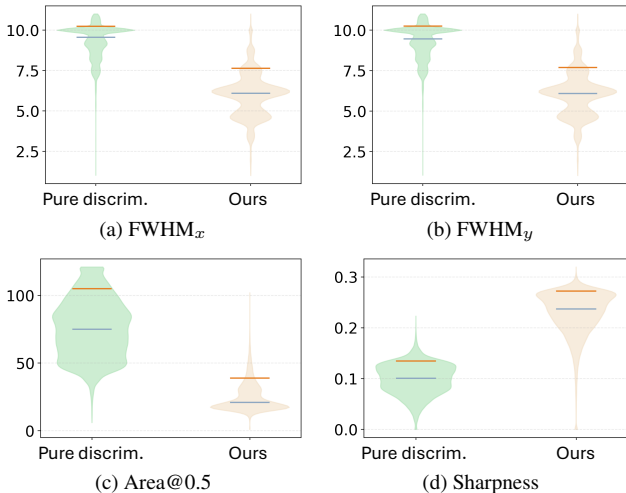


Figure 5. Vertex peak-shape comparison between the *pure discriminative* baseline and our *distributional reconstruction*. Lower values of FWHM and Area@0.5 indicate sharper and more compact peaks, while higher Sharpness reflects stronger local contrast. The blue/red bar denotes the median/90th percentile.

Table 6. Summary statistics (median and 90th percentile) of vertex peak-shape metrics.

Metric	Pure discrim.		Ours (dist. model)	
	Median	$P_{90}$	Median	$P_{90}$
FWHM $_x$ $\downarrow$	9.55	10.23	<b>6.09</b>	<b>7.64</b>
FWHM $_y$ $\downarrow$	9.46	10.25	<b>6.09</b>	<b>7.70</b>
Area@0.5 $\downarrow$	75.0	105.0	<b>21.0</b>	<b>39.0</b>
Sharpness $\uparrow$	0.10	0.14	<b>0.24</b>	<b>0.27</b>

*criminative*) adopting the ViTPose [37] design as a strong baseline. We analyze vertex peak shapes using three intuitive metrics—*FWHM* (peak width), *Area@0.5* (size of high-response region), and *Sharpness* (local contrast)—with full computation details provided in the supplementary material. As shown in Fig. 5 and Table 6, the diffusion-based reconstruction yields sharper, more isotropic, and spatially compact peaks (smaller FWHM, lower high-response area, and higher sharpness), whereas the discriminative head produces broad or band-like responses (see Fig. 4). These results demonstrate that our approach effectively handles the challenges of weak visual cues and smooth boundaries relying on cartographic conventions highlighted in Sec. 1.

We also evaluate robustness under varying NMS thresh-

Table 7. Ablation of Topology-consistency on the reconstruction stage. Metrics are averaged over DP tolerances  $\varepsilon \in \{1, 2, 3, 4\}$ .

Method	Gap $\downarrow$	Inter $\downarrow$	Intra $\downarrow$	Shared $\uparrow$
No PSLG + DP (w/o VSS)	1.04	0.14	0.00	15.38
<b>PSLG + DP (w/o VSS)</b>	<b>0.00</b>	<b>0.00</b>	<b>0.00</b>	<b>100.00</b>

olds. The distributional model shows minimal variance across all polygonal metrics, whereas the discriminative baseline fluctuates notably (detailed in the supplementary).

**Ablation on Topological Reconstruction.** This evaluates the effectiveness of (i) the planar structural precondition established by the *overdense PSLG construction*, and (ii) the geometric simplification enabled by the *vertex-guided subset selection* (VSS). All variants share the same segmentation and vertex priors ( $\hat{M}, \hat{Y}$ ) for fair comparison.

**(i) Importance of the planar structural precondition.** We compare the full PSLG-based reconstruction (“PSLG + DP, without VSS”) against a variant that omits the PSLG and polygonizes each semantic class independently from its mask boundaries (“No PSLG + DP, without VSS”). The goal is to validate the necessity of building a globally planar straight-line graph as required by Proposition 1. As shown in Table 7, removing the PSLG destroys the planar structural precondition, leading to severe violations in shared edge consistency. In contrast, the PSLG enforces a single global planar graph on which faces are labeled, serving as the essential precondition for realizing Proposition 1 and ensuring topology consistency *by design*.

**(ii) Effect of VSS.** We also compare our vertex-guided subset selection (VSS) with the traditional geometry-only simplification algorithm Douglas–Peucker (DP) [5]. While DP minimizes geometric deviation, it is highly sensitive to the tolerance parameter and lacks data-driven saliency. Our VSS leverages learned vertices for adaptive keypoint preservation and yields lower redundancy at comparable or lower geometric error (see supplementary for details).

## 7. Conclusion

We presented **ACPV-Net**, the first fully automatic framework for seamless and topologically consistent vector basemap generation from aerial imagery. Departing from existing single-class polygonal outline extraction methods, our approach performs all-class polygonal vectorization in a single run. On the new **Deventer-512** benchmark, ACPV-Net achieves gap-/overlap-free topology with shared-edge consistency, and consistently outperforms strong single-class baselines across all land-cover classes. It also generalizes to single-class polygonal extraction, achieving the best results on the WHU-Building dataset. We believe this work represents an important step toward fully automated, large-scale, and topologically consistent vector map generation in remote sensing.

## 8. Acknowledgment

This publication is part of the project “Learning from old maps to create new ones”, with project number 19206 of the Open Technology Programme, which is financed by the Dutch Research Council (NWO), The Netherlands. We thank the members of the project for their support in data preparation.

## References

- [1] Isprs 2d semantic labeling - potsdam. <https://www.isprs.org/resources/datasets/benchmarks/UrbanSemLab/2d-sem-label-potsdam.aspx>, . Accessed: 2025-11-10. 5
- [2] Isprs 2d semantic labeling - vaihingen. <https://www.isprs.org/resources/datasets/benchmarks/UrbanSemLab/2d-sem-label-vaihingen.aspx>, . Accessed: 2025-11-10. 5
- [3] Yeshwanth Kumar Adimoolam, Charalambos Poullis, and Melinos Averkiou. Pix2poly: A sequence prediction method for end-to-end polygonal building footprint extraction from remote sensing imagery. In *2025 IEEE/CVF Winter Conference on Applications of Computer Vision (WACV)*, pages 8484–8493. IEEE, 2025. 3
- [4] Yizi Chen, Joseph Chazalon, Edwin Carlinet, Minh Ôn Vũ Ngoc, Clément Mallet, and Julien Perret. Automatic vectorization of historical maps: A benchmark. *Plos one*, 19(2):e0298217, 2024. 3
- [5] David H Douglas and Thomas K Peucker. Algorithms for the reduction of the number of points required to represent a digitized line or its caricature. *Cartographica: the international journal for geographic information and geovisualization*, 10(2):112–122, 1973. 3, 8
- [6] Esri. Geodatabase topology rules and fixes for polygon features. <https://pro.arcgis.com/en/pro-app/latest/help/editing/geodatabase-topology-rules-for-polygon-features.htm>, 2025. Includes rules such as *Must Not Overlap* and *Must Not Have Gaps*. 1, 3
- [7] Esri. Vector basemaps — overview. <https://links.esri.com/agol-help/vector-basemaps-group>, 2025. ArcGIS Online official overview of Esri Vector Basemaps. 1
- [8] Geonovum. Basisregistratie grootschalige topografie gegevenscatalogus bgt 1.2, 2020. Accessed: 2025-04-02. 1
- [9] Nicolas Girard, Dmitriy Smirnov, Justin Solomon, and Yuliya Tarabalka. Polygonal building extraction by frame field learning. In *Proceedings of the IEEE/CVF Conference on Computer Vision and Pattern Recognition*, pages 5891–5900, 2021. 2, 3, 5, 6, 7
- [10] Google. How google maps is made. <https://blog.google/intl/en-mena/product-updates/explore-get-answers/how-google-maps/>, 2022. Updated official blog post on map-building practices. 1
- [11] Google. Vector map features — maps javascript api. <https://developers.google.com/maps/documentation/javascript/vector-map>, 2025. Describes the vector basemap delivery/rendering (client-side WebGL). 1
- [12] Joachim Höhle. Generating topographic map data from classification results. *Remote Sensing*, 9(3):224, 2017. 1
- [13] International Organization for Standardization. Iso 19125-1:2004 — geographic information — simple feature access — part 1: Common architecture. <https://cdn.standards.iteh.ai/samples/40114/17e00cdeb36e49fea340185d746e4a20/ISO-19125-1-2004.pdf>, 2004. 1, 3
- [14] Shunping Ji, Shiqing Wei, and Meng Lu. Fully convolutional networks for multisource building extraction from an open aerial and satellite imagery data set. *IEEE Transactions on geoscience and remote sensing*, 57(1):574–586, 2018. 5, 6
- [15] Weiqin Jiao, Claudio Persello, and George Vosselman. Polyr-cnn: R-cnn for end-to-end polygonal building outline extraction. *ISPRS Journal of Photogrammetry and Remote Sensing*, 218:33–43, 2024. 2, 3
- [16] Weiqin Jiao, Hao Cheng, George Vosselman, and Claudio Persello. Ldpoly: Latent diffusion for polygonal road outline extraction in large-scale topographic mapping. *ISPRS Journal of Photogrammetry and Remote Sensing*, 230:820–842, 2025. 3
- [17] Weiqin Jiao, Hao Cheng, George Vosselman, and Claudio Persello. Roipoly: Vectorized building outline extraction using vertex and logit embeddings. *ISPRS Journal of Photogrammetry and Remote Sensing*, 224:317–328, 2025. 2, 3
- [18] Alexander Kent. Topographic maps: methodological approaches for analyzing cartographic style. *Journal of Map & Geography Libraries*, 5(2):131–156, 2009. 1
- [19] Alexander J Kent and Anja Hopfstock. Topographic mapping: past, present and future. *The Cartographic Journal*, 55(4):305–308, 2018. 1
- [20] Yuxuan Li, Qibin Hou, Zhaohui Zheng, Ming-Ming Cheng, Jian Yang, and Xiang Li. Large selective kernel network for remote sensing object detection. In *Proceedings of the IEEE/CVF international conference on computer vision*, pages 16794–16805, 2023. 3
- [21] Yuxuan Li, Xiang Li, Yimain Dai, Qibin Hou, Li Liu, Yongxiang Liu, Ming-Ming Cheng, and Jian Yang. Lsknet: A foundation lightweight backbone for remote sensing: Y. li et al. *International Journal of Computer Vision*, 133(3):1410–1431, 2025. 3
- [22] Tianyu Lin, Zhiguang Chen, Zhonghao Yan, Weijiang Yu, and Fudan Zheng. Stable diffusion segmentation for biomedical images with single-step reverse process. In *International Conference on Medical Image Computing and Computer-Assisted Intervention*, pages 656–666. Springer, 2024. 3
- [23] Yue Liu, Yunjie Tian, Yuzhong Zhao, Hongtian Yu, Lingxi Xie, Yaowei Wang, Qixiang Ye, Jianbin Jiao, and Yunfan Liu. Vmamba: Visual state space model. *Advances in neural information processing systems*, 37:103031–103063, 2024. 3
- [24] Emmanuel Maggiori, Yuliya Tarabalka, Guillaume Charpiat, and Pierre Alliez. Can semantic labeling methods generalize to any city? the inria aerial image labeling benchmark.

- In *2017 IEEE International geoscience and remote sensing symposium (IGARSS)*, pages 3226–3229. IEEE, 2017. 5
- [25] Yu Meng, Ligao Deng, Zhihao Xi, Jiansheng Chen, Jingbo Chen, Anzhi Yue, Diyou Liu, Kai Li, Chenhao Wang, Kaiyu Li, et al. Irsamap: Towards large-scale, high-resolution land cover map vectorization. *IEEE Transactions on Geoscience and Remote Sensing*, 2025. 3
- [26] Faculty of Geo-Information Science and University of Twente Earth Observation (ITC). Concept page 81728: [title of the concept as shown on the page]. <https://lbtb.itc.utwente.nl/page/498/concept/81728>. Accessed: November 9, 2025. 3
- [27] Open Geospatial Consortium. Simple feature access — part 1: Common architecture (iso 19125-1). <https://www.ogc.org/publications/standard/sfa/>, 2011. 1, 3
- [28] SJ Oude Elberink. Acquisition of 3d topography: automated 3d road and building reconstruction using airborne laser scanner data and topographic maps. 2010. 1
- [29] Sida Peng, Wen Jiang, Huaijin Pi, Xiuli Li, Hujun Bao, and Xiaowei Zhou. Deep snake for real-time instance segmentation. In *Proceedings of the IEEE/CVF conference on computer vision and pattern recognition*, pages 8533–8542, 2020. 3, 5, 6, 7
- [30] Robin Rombach, Andreas Blattmann, Dominik Lorenz, Patrick Esser, and Björn Ommer. High-resolution image synthesis with latent diffusion models. In *Proceedings of the IEEE/CVF conference on computer vision and pattern recognition*, pages 10684–10695, 2022. 2, 3, 4, 7
- [31] Chenhao Wang, Zhihao Xi, Diyou Liu, Yuman Feng, Yupeng Deng, Kai Li, Jingbo Chen, Jiansheng Chen, and Yu Meng. Pcp: A prompt-based cartographic-level polygonal vector extraction framework for remote sensing images. *IEEE Transactions on Geoscience and Remote Sensing*, 2025. 3
- [32] Jingdong Wang, Ke Sun, Tianheng Cheng, Borui Jiang, Chaorui Deng, Yang Zhao, Dong Liu, Yadong Mu, Mingkui Tan, Xinggang Wang, et al. Deep high-resolution representation learning for visual recognition. *IEEE transactions on pattern analysis and machine intelligence*, 43(10):3349–3364, 2020. 3
- [33] Junjue Wang, Zhuo Zheng, Ailong Ma, Xiaoyan Lu, and Yanfei Zhong. Loveda: A remote sensing land-cover dataset for domain adaptive semantic segmentation. In *Proceedings of the Neural Information Processing Systems Track on Datasets and Benchmarks*. Curran Associates, Inc., 2021. 5
- [34] Libo Wang, Rui Li, Ce Zhang, Shenghui Fang, Chenxi Duan, Xiaoliang Meng, and Peter M Atkinson. Unetformer: A unet-like transformer for efficient semantic segmentation of remote sensing urban scene imagery. *ISPRS Journal of Photogrammetry and Remote Sensing*, 190:196–214, 2022. 3
- [35] Xue Xia, Tao Zhang, Magnus Heitzler, and Lorenz Hurni. Vectorizing historical maps with topological consistency: A hybrid approach using transformers and contour-based instance segmentation. *International Journal of Applied Earth Observation and Geoinformation*, 129:103837, 2024. 3
- [36] Bowen Xu, Jiakun Xu, Nan Xue, and Gui-Song Xia. Hisup: Accurate polygonal mapping of buildings in satellite imagery with hierarchical supervision. *ISPRS Journal of Photogrammetry and Remote Sensing*, 198:284–296, 2023. 2, 3, 5, 6, 7
- [37] Yufei Xu, Jing Zhang, Qiming Zhang, and Dacheng Tao. Vitpose: Simple vision transformer baselines for human pose estimation. *Advances in neural information processing systems*, 35:38571–38584, 2022. 8
- [38] Bingnan Yang, Mi Zhang, Zhan Zhang, Zhili Zhang, and Xiangyun Hu. Topdig: Class-agnostic topological directional graph extraction from remote sensing images. In *Proceedings of the IEEE/CVF Conference on Computer Vision and Pattern Recognition*, pages 1265–1274, 2023. 2, 3, 5, 6, 7
- [39] Tao Yang, Rongyuan Wu, Peiran Ren, Xuansong Xie, and Lei Zhang. Pixel-aware stable diffusion for realistic image super-resolution and personalized stylization. In *European conference on computer vision*, pages 74–91. Springer, 2024. 2, 3, 4, 7
- [40] Fahong Zhang, Yilei Shi, and Xiao Xiang Zhu. Global collinearity-aware polygonizer for polygonal building mapping in remote sensing. *IEEE Transactions on Geoscience and Remote Sensing*, 2025. 2, 3, 5, 6, 7
- [41] Lvmin Zhang, Anyi Rao, and Maneesh Agrawala. Adding conditional control to text-to-image diffusion models. In *Proceedings of the IEEE/CVF international conference on computer vision*, pages 3836–3847, 2023. 2, 3, 4, 7
- [42] Wufan Zhao, Claudio Persello, and Alfred Stein. Building outline delineation: From aerial images to polygons with an improved end-to-end learning framework. *ISPRS journal of photogrammetry and remote sensing*, 175:119–131, 2021. 2, 3
- [43] Yibo Zhao, Liang Peng, Yang Yang, Zekai Luo, Hengjia Li, Yao Chen, Zheng Yang, Xiaofei He, Wei Zhao, Qinglin Lu, et al. Local conditional controlling for text-to-image diffusion models. In *Proceedings of the AAAI Conference on Artificial Intelligence*, pages 10492–10500, 2025. 2, 3, 4, 7
- [44] Qinfeng Zhu, Yuanzhi Cai, Yuan Fang, Yihan Yang, Cheng Chen, Lei Fan, and Anh Nguyen. Samba: Semantic segmentation of remotely sensed images with state space model. *Heliyon*, 10(19), 2024. 3
- [45] Stefano Zorzi and Friedrich Fraundorfer. Re: Polyworld—a graph neural network for polygonal scene parsing. In *Proceedings of the IEEE/CVF International Conference on Computer Vision*, pages 16762–16771, 2023. 3
- [46] Stefano Zorzi, Shabab Bazrafkan, Stefan Habenschuss, and Friedrich Fraundorfer. Polyworld: Polygonal building extraction with graph neural networks in satellite images. In *Proceedings of the IEEE/CVF Conference on Computer Vision and Pattern Recognition*, pages 1848–1857, 2022. 2, 3